ACS APPLIED MATERIALS & INTERFACES

www.acsami.org

Research Article

The Antibody-Free Recognition of Cancer Cells Using Plasmonic Biosensor Platforms with the Anisotropic Resonant Metasurfaces

Zhang Zhang,[#] Maosheng Yang,[#] Xin Yan, Xinyue Guo, Jie Li, Yue Yang, Dequan Wei, Longhai Liu, Jianhua Xie, Yufei Liu, Lanju Liang,* and Jianquan Yao*

Cite This: *ACS Appl. Mater. Interfaces* 2020, 12, 11388−11396

Read Online

ACCESS | Metrics & More | Article Recommendations | Supporting Information

ABSTRACT: It is vital and promising for portable and disposable biosensing devices to achieve on-site detection and analysis of cancer cells. Although traditional labeling techniques provide an accurate quantitative measurement, the complicated cell staining and high-cost measurements limit their further development. Here, we demonstrate a nonimmune biosensing technology. The plasmonic biosensors, which are based on anisotropic resonant split ring resonators in the terahertz range, successfully realize the antibody-free recognition of cancer cells. The dependences of Δf and the fitted phase slope on the cancer cell concentration at different polarizations give new perspective in hexagonal radar maps. The results indicate that the lung cancer cell A549 and liver cancer cell HepG2 can be distinguished and determined simply based on the enclosed shapes in the radar maps without any antibody introduction. The minimum concentration of identification reduces to as low as 1×10^4 cells/mL and such identification can be kept valid in a wide range of cell concentration, ranging from 10^4 to 10^5. The construction of two-dimensional extinction intensity cards of corresponding cancer cells based on the wavelet transform method also supplies corresponding information for the antibody-free recognition and determination of two cancer cells. Our plasmonic metasurface biosensors show a great potential in the determination and recognition of label-free cancer cells, being an alternative to nonimmune biosensing technology.

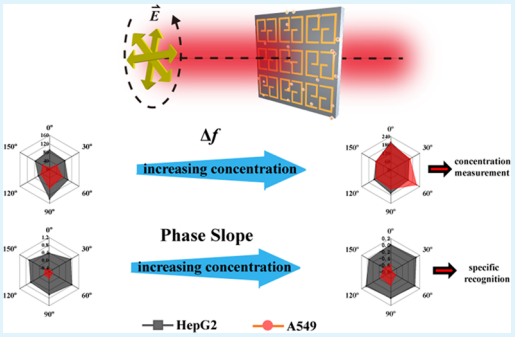

KEYWORDS: *metasurfaces, terahertz, antibody-free biosensing, cancer cells, continuous wavelet transform*

INTRODUCTION

Metamaterials, consisting of artificial "meta-atoms" that can resonate with incident electromagnetic waves, bring new insight into light−matter interaction.[1−4] Their extraordinary optical properties such as negative refractive index, inverse Doppler effect, and diffraction, which are unachievable in natural materials, bring an unprecedented advancement in various fields including transformation optics, communication engineering, and hologram imaging.[5−9] Metasurfaces, the two-dimensional equivalent metamaterials, are recently proposed and are attractive in the research community.[10−14] By periodically arranging planar meta-atoms such as split ring resonators (SRRs), the specific surface plasmonic resonances can be induced by incident electromagnetic waves.[15] More importantly, metasurfaces are much more sensitive to the change in local environment due to the strong localized fields in the near-field, exhibiting a great potential in biosensing, especially for the fast and accurate detection of cancer cells. Recently, several works about the biosensors based on the metasurfaces have been reported.[16−23] By measuring the shift Δf in the frequency range of resonant positions, the concentration change in cells can be detected. Compared with current labeling methods (e.g., flow cytometer), metasurface biosensors (MBs) are an alternative to avoid the complicated cell staining, greatly simplifying the test procedure and lowering the test cost. Despite the success of MBs in cell measurements, they still suffer from an inevitable defect, that is, surface modification by immobilizing antibody. The specific recognition of antigen to antibody contributes to the selective detection of such immune biosensors, but the limited modification area and deficient device-recycling restrict the MBs toward higher performance. Especially, for the measurement of cancer cells, the lack of available antibody makes the differentiating for different types of cancer cells hard based on traditional immune biosensors. The MB platform that can distinguish the label-free cancer cells without the antibody introduction turns out to be urgent.

The plasmonic metasurfaces with SRRs, as well known, can exhibit anisotropic resonant response to electromagnetic waves by specifically designing their asymmetric configuration. The polarization-dependent resonant characteristics extend the

Received: January 3, 2020
Accepted: February 20, 2020
Published: February 20, 2020

https://dx.doi.org/10.1021/acsami.0c00095
ACS Appl. Mater. Interfaces 2020, 12, 11388−11396

biosensing criteria into other polarization components. The component resonances may reveal certain matter-related response parameters that are unexplored before. Such anisotropic features supply abundant biosensing information because it helps us to acquire multidimensional information for the wave−matter interaction from a more comprehensive perspective. On the other hand, terahertz (THz) waves are characterized by the low average power and nonionization, being attractive to the photonic sensing technology.[24−26] Notably, since the frequency location of most intermolecular interactions is in the THz range, the THz waves show great promise in biological applications.[27] Besides, as the majority of biological matters comprise chiral molecular units such as amino acids and sugars, the biomacromolecules formed from these units also exhibit chirality on molecular scales, which can cause optical rotation.[28] In other words, the orientation of the polarization plane about the optical axis of linearly polarized light would be rotated when THz waves travel through chiral materials. For this reason, the MBs with anisotropic resonant parameters combined with chiral biomatters exhibit specialized polarization-dependent features, contributing to the antibody-free recognition of cancer cells.

Here, we propose a nonimmune biosensing platform based on anisotropic resonant metasurfaces for antibody-free recognition of cancer cells. The mirror-asymmetric design of plasmonic SRRs enables the MBs to generate specific resonant response to THz waves with the change in polarization. In experiments, two kinds of cancer cells, A549 and HepG2, are cultured on MBs. By measuring the THz transmission spectra, the dependences of Δf and the fitted phase slope (FPS) on the cancer cell concentration at different polarization cases are acquired. Some anomalous features such as the decreasing stage in the Δf with the increase in cell concentration are observed, indicating the possible cell state distinction between different concentrations. When the cell concentration reaches the highest (5×10^5 cells/mL), the Δf in all polarization cases reach the maximum in our measurements, which are up to 213 GHz for A549 cells and 198 GHz for HepG2 cells. More importantly, in FPS radar maps, the enclosed areas of HepG2 cells are always larger than those of A549 cells. Such an insensitive feature to cell concentration enables to directly differentiate two kinds of cancer cells only based on the significant difference in the enclosed shapes in the radar maps without any antibody introduction and cellular staining. The minimum concentration of identification reduces to as low as 1×10^4 cells/mL and such identification can be kept valid in a wide range of cell concentration, ranging from 10^4 to 10^5 Finally, a set of standard two-dimensional extinction intensity cards of cancer cells have been built based on the continuous wavelet transform (CWT) method. Through matching the measured extinction intensity graphs of cells with the standard cards, the recognition and determination of label-free A549 and HepG2 cancer cells can be further affirmed. Our plasmonic MBs realize the fast detection and antibody-free recognition of A549 and HepG2 cancer cells, being a potential alternative to the future nonimmune biosensing technology.

EXPERIMENTAL SECTION: SAMPLES AND PROCEDURES

The mirror-asymmetric configuration of SRRs is designed to induce the anisotropic resonances, as seen in Figure 1a. The structure of unit cell is shown in Figure 1b; the detailed structural parameters are given: P = 63 μm, l = 58 μm, g = 4 μm, d = 14 μm, and h = 10 μm.

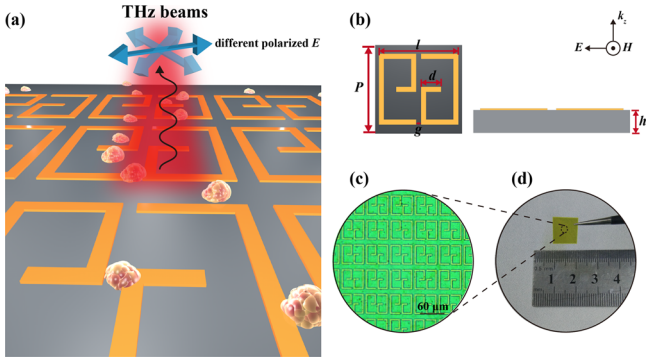

Figure 1. (a) Schematic illustration of MB platforms: THz beams penetrates through the devices on which cancer cells were cultured. (b) Design of the unit structure: P = 63 μm, l = 58 μm, g = 4 μm, d = 14 μm, and h = 10 μm. (c) Photomicrograph of the fabricated metasurface in a small zone. (d) Physical photograph of flexible MBs.

The metallic linewidth is 3.6 μm. The SRR array is supported on the polyimide (PI) substrate. The flexible feature makes the devices more effective and accessible, providing opportunities for rapid detection of cancer cells. The photomicrograph and physical photograph of MBs are shown in Figure 1c,d, respectively. To demonstrate the biosensing performance of MBs, two kinds of cancer cells, nonsmall lung cancer cells A549 and human hepatocellular carcinomas HepG2, are cultured on the platforms. The main steps including sample fabrication and cell culturing method are schematically displayed in Figure 2. The rotation sample holder controls the polarization angle of incident THz waves. The patterns of SRRs are acquired by standard photolithography, and cell culturing follows the adherent cell culturing method. More details can be found in the Experimental Section.

RESULTS AND DISCUSSION

First, the THz spectra of fabricated metasurfaces are measured under different polarization angles of incident waves, as seen in Figure 3. With the polarization angle θ changing from 0 to 150°, the transmission response of the metasurface also varies. Such distinct resonances indicate the polarization-dependent feature of proposed MBs. As can be seen, three obvious resonant positions are observed when the electric field is oriented along the y axis (Figure 3a) and the resonance only remains one when θ is 150° (Figure 3f). Meanwhile, it can be found from Figure 3a−f that the simulation results agree well with experiments except for a little discrepancy in transmission intensity, which may be caused by the fabrication error and larger dielectric loss of samples. The electric-field distributions at each resonance are also monitored and given in insets. When the polarization changes, the corresponding resonant mode transforms as well. These specific modes induced by different polarized waves originate from the component of excited waves. As polarization rotates, the excited field along the y axis is in fact a component of the electric field. Such a component change demonstrates the anisotropic resonance property of the metasurface. The extended resonant features provide an opportunity to acquire more resonance parameters, contributing to a more accurate determination and antibody-free recognition.

The experimental measurements under E_y-polarized THz waves are taken as an example and shown in Figure 4. As mentioned before, three resonant dips are induced under this condition, as shown in Figure 4a. Six concentrations of HepG2 cells are cultured on MBs, and three of them are shown in Figure 4a−c. The corresponding photomicrographs are also

https://dx.doi.org/10.1021/acsami.0c00095
ACS Appl. Mater. Interfaces 2020, 12, 11388−11396

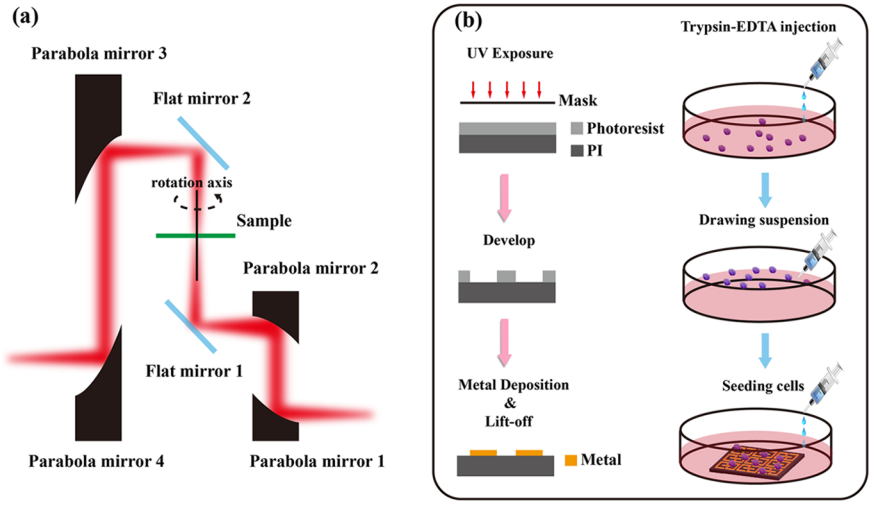

Figure 2. (a) Optical path installation of THz measurement system. (b) Main steps of sample fabrication (left column) and cell culturing process (right column).

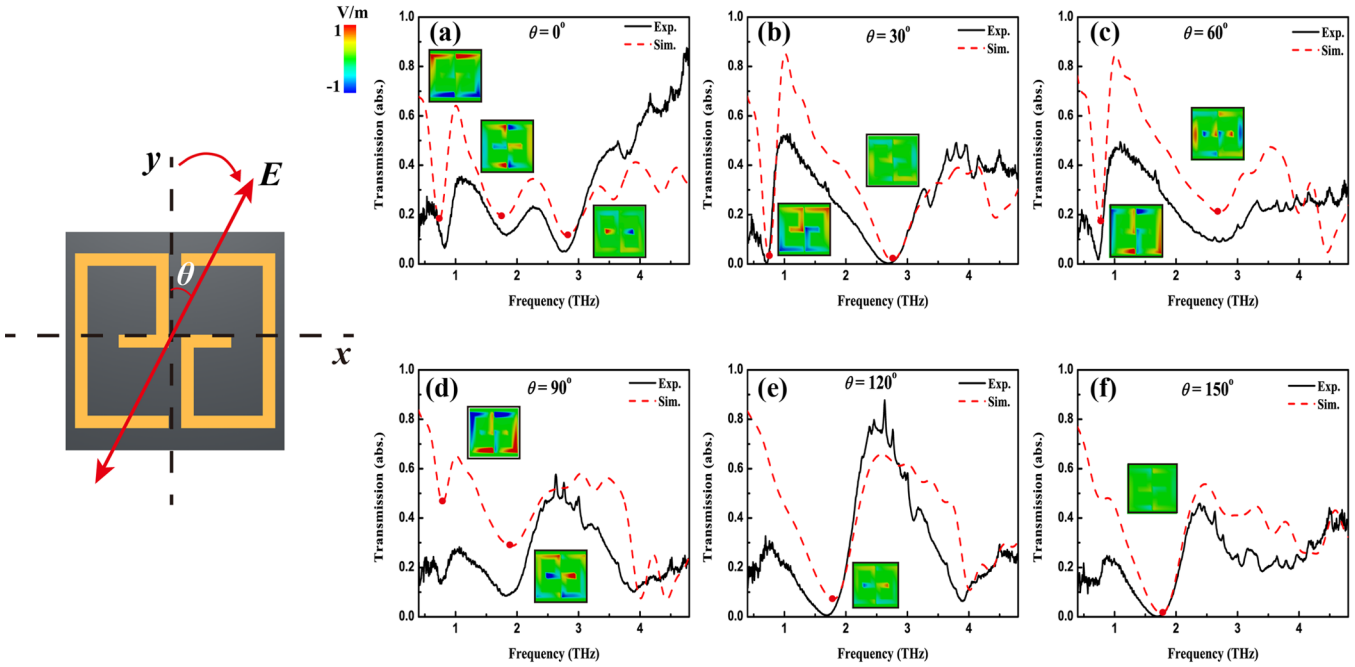

Figure 3. Transmission spectrum of the metasurface under the polarization angles of (a) 0, (b) 30, (c) 60, (d) 90, (e) 120, (f) 150°. The corresponding electric-field distributions at each resonant position are given in insets.

inserted. All measurement results of six concentrations can be found in the Supporting Information, Figure S1. Obviously, after the cancer cell culturing, the transmission spectra of samples slightly change and three main resonant dips redshift in the frequency range. In order to acquire the dependence of the frequency shift Δf on the cell concentration, the corresponding shift values of three resonant dips are extracted (Figure 4d). Notably, owing to the fabrication error and nonspecific biomolecule absorption, the resonant frequency of each bare sample may not appear at the same position and thus leads to severe false positive issues. In order to obtain the accurate Δf, every bare sample is first measured before culturing the cells. The corresponding resonant frequency is represented as $f_i^{(\mathrm{bare})}$ (i = 1, 2, 3, 4, 5, 6). After the cells are cultured on every sample, the resonant frequencies are measured again and recorded as $f_i^{(\mathrm{cells})}$. Thus, the relative Δf is defined as $\Delta f = f_i^{(\mathrm{cells})} - f_i^{(\mathrm{bare})}$. It should be mentioned that all bare samples were taken out from the culturing medium followed by the spectral measurements. In other words, the influences resulting from other nonspecific biomolecules are measured by bare samples. By subtracting the resonant frequency of bare samples from that of samples with cancer cells, the effects introduced by absorbed nonspecific biomolecules were removed. The results shown in Figure 4d imply that the Δf of three resonant dips reach the highest when the cell concentration increases to the maximum of 5×10^5 cells/mL. In addition, a higher resonance exhibits a higher Δf under the same cell concentration. At dip 3, the highest Δf is up to 198 GHz. However, the Δf experiences a descending stage when the cell concentration arrives at 5×10^4 and 3×10^5 cells/mL. In contrast to the continuously increasing Δf with the increase in cell concentration in previous works we

https://dx.doi.org/10.1021/acsami.0c00095
ACS Appl. Mater. Interfaces 2020, 12, 11388−11396

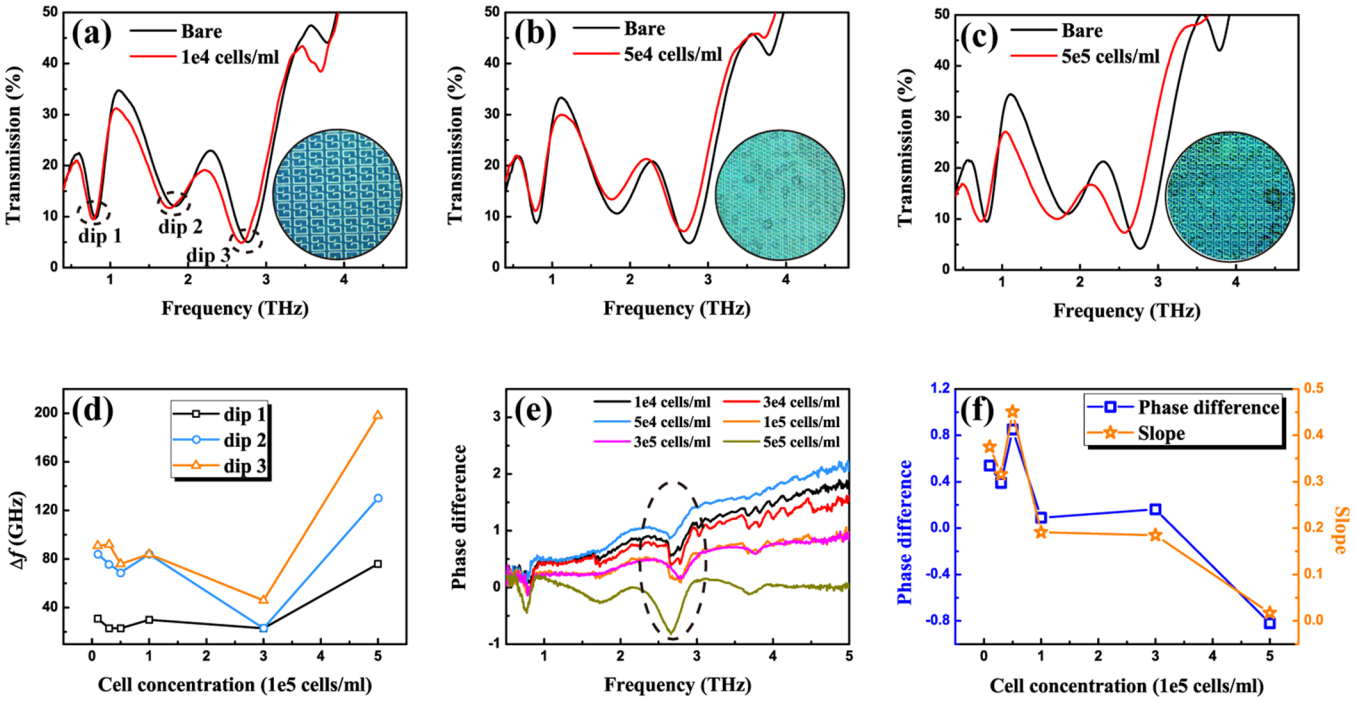

Figure 4. (a–c) Experimental transmission spectra of MBs at different cancer cell concentrations increasing at 1×10^4, 5×10^4, and 5×10^5 cells/mL under E_y-polarized THz waves. (d) Dependence of Δf on cell concentration increasing from 1×10^4 to 5×10^5 cells/mL. (e) Phase difference between the sample with and without cancer cells under every cell concentration. (f) Dependence of extracted phase differences and fitted phase slopes on cancer cell concentration.

reported,[20,29,30] such a variation in Δf is anomalous. Compared with the oral cancer cells investigated in previous works, the HepG2 cells have a larger cell volume. It can be clearly observed from insets in Figure 4b and Figure S1e that the descending Δf mainly emerges at the two concentrations where larger cells are scattered on. It is inferred that the mode coupling of SRRs in the near-field may be greatly disturbed by cancer cells with larger cell volume. The effective permittivity of dielectric environment produces an anomalous response. It should be mentioned that such descending Δf may appear in the case of a lower cell concentration in which the cell size and distribution position become dominant. Meanwhile, in a higher cell concentration on MBs, the Δf would increase prominently with the increment in cells, which agrees with our previous observations. It is the uncertainty created by cell state that makes the request for additional information to accurately determine the cancer cells in a low concentration. Other spectral parameters should be considered to obtain more biological information. The phase difference of MBs is measured for every cell concentration as seen in Figure 4e where the dependence of phase difference on frequency is quasi-linear except for a specific dip in the frequency range at about 2.73 THz. Consequently, the linear fitted phase slope (FPS) and the phase difference values at the dip can be considered as another biosensing criteria for MB platforms. It is observed from Figure 4f that the phase difference and FPS have almost the same variation with the increase in cancer cells. Meanwhile, slight decreases in phase difference and FSP are observed with the cell concentration. These results imply that the phase is also altered after the introduction of cells. Such a phase information and Δf compose a multidimensional biosensing, enhancing the determination and the recognition of cancer cells by using plasmonic MBs.

The principle of metasurface biosensing platforms can be interpreted by the perturbation theory. Based on two curl equations related $E(r)$ to $H(r)$ in electromagnetic dynamics, the condition on the electric field is written as

$$\nabla \times \nabla \times E(r) = \left(\frac{\omega}{c}\right)^2 \varepsilon(r) E(r) \tag{1}$$

By applying the perturbation procedure to eq 1, we obtain a simple formula for the frequency shift $\Delta\omega$ that results from a small perturbation $\Delta\varepsilon$ of the dielectric function

$$\Delta\omega = -\frac{\omega}{2} \frac{\int d^3 r \Delta\varepsilon(r) |E(r)|^2}{\int d^3 r \varepsilon(r) |E(r)|^2} + O(\Delta\varepsilon^2) \tag{2}$$

Consider the case of a material with a refractive index $n = \sqrt{\varepsilon}$ in which the index is perturbed in some regions by an amount Δn. The volume integral in the numerator of the equation (Figure S3) has nonzero contributions only from the perturbed regions. Writing $\Delta\varepsilon \approx \varepsilon 2\Delta n/n$ and supposing that $\Delta n/n$ is the same in all the perturbed regions (and can therefore be brought outside the integral), we obtain

$$\frac{\Delta\omega}{\omega} \approx -\frac{\Delta n}{n} \times P \tag{3}$$

P represents the fraction of $\int \varepsilon |E|^2$ in the perturbed regions. It can be seen that the fractional change in frequency is equal to the fractional change in index multiplied by the fraction of the electric-field energy inside the perturbed regions. In other words, if the dielectric environment in the near-field of the SRR surface changed due to the introduction of biological cells, the resonant frequency also generates a shift in the frequency range.

Due to the mirror-asymmetric designs of SRRs, the resonant response to THz waves is extended with the change in

https://dx.doi.org/10.1021/acsami.0c00095
ACS Appl. Mater. Interfaces 2020, 12, 11388–11396

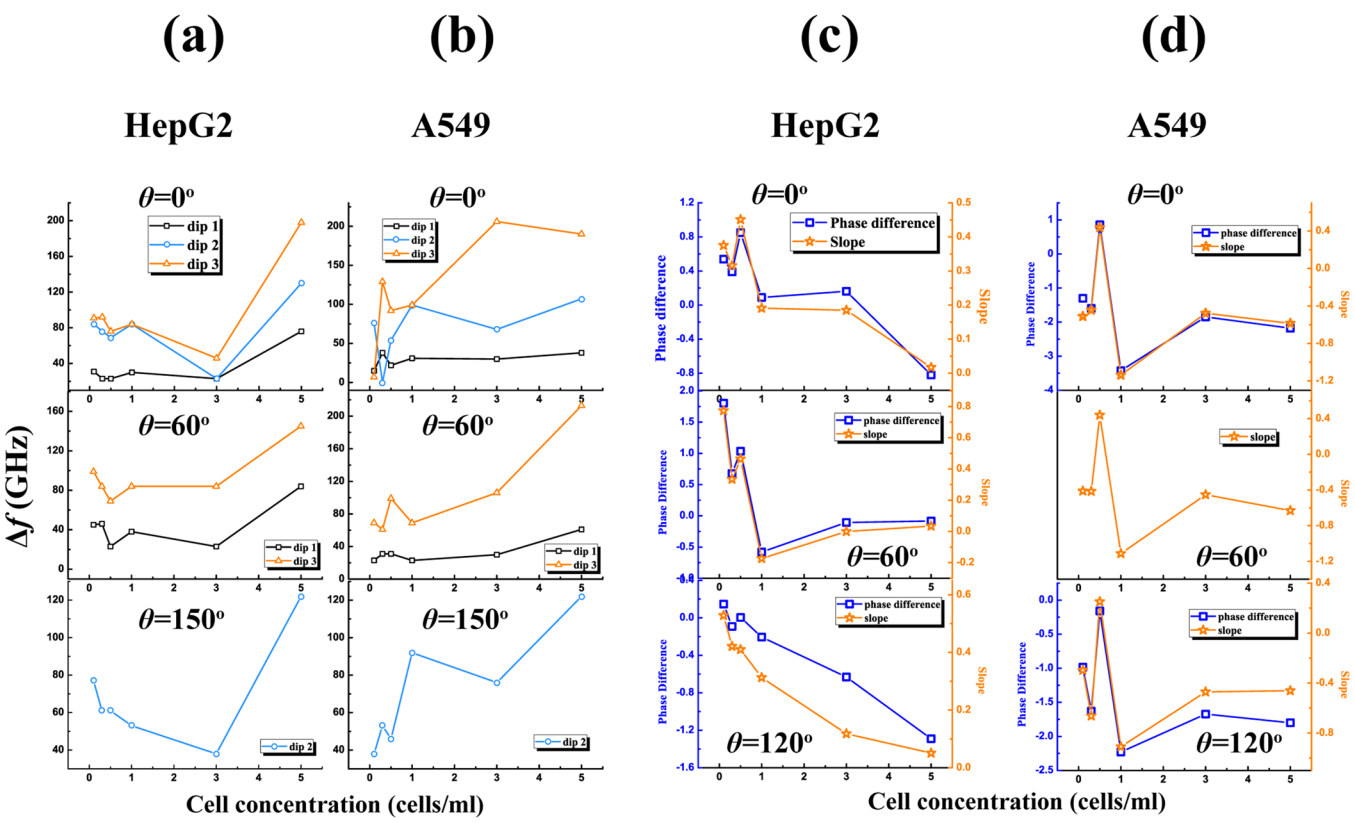

Figure 5. (a, b) Dependence of Δf on cell concentration in certain polarization cases for (a) HepG2 cells and (b) A549 cells. (c, d) Dependence of phase difference and FPS value on cell concentration in certain polarization cases for (c) HepG2 cells and (d) A549 cells.

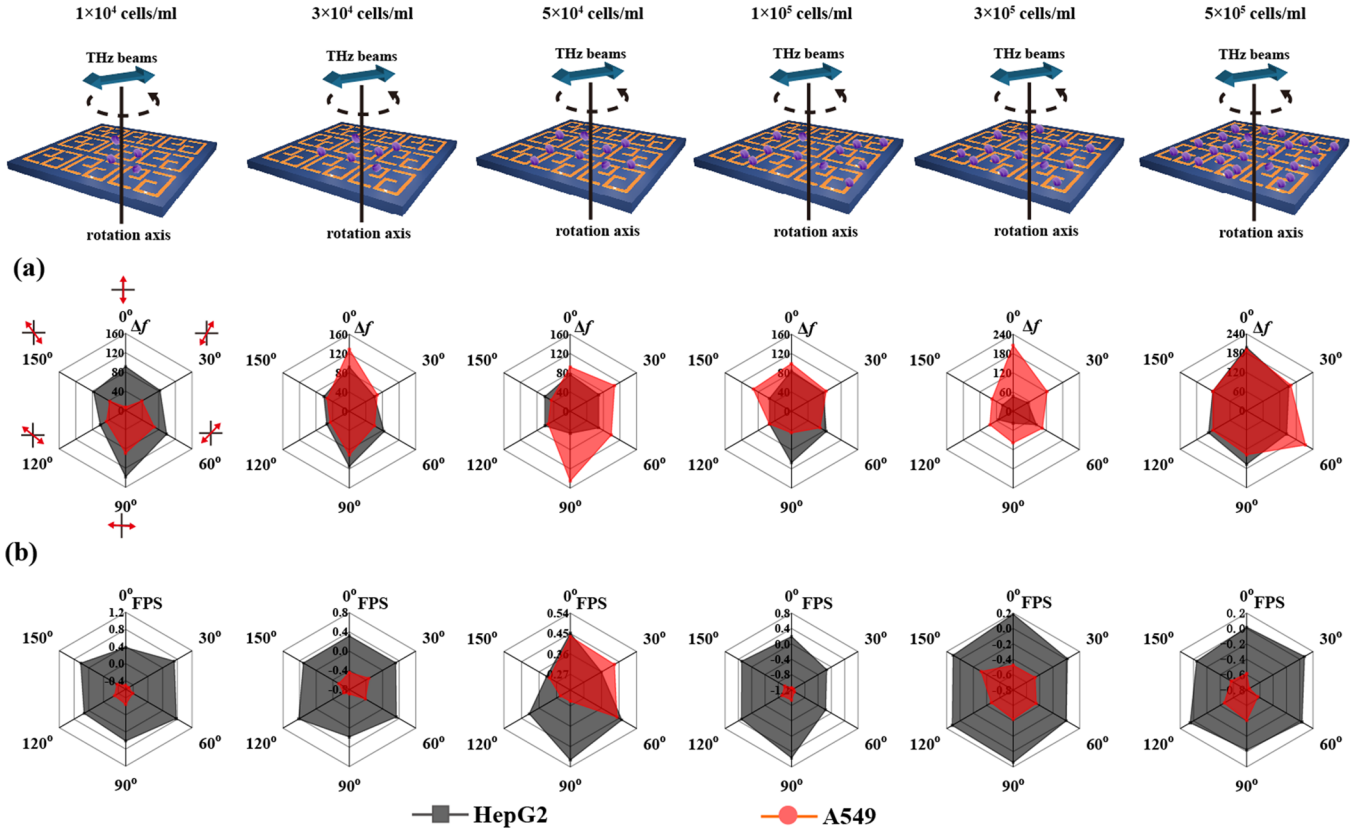

Figure 6. (a, b) Hexagonal radar maps of (a) Δf and (b) fitted phase slope at each cell concentration. The A549 and HepG2 cancer cells are represented by red and black solid shapes, respectively. Every vertex in hexagonal radar maps stands for the different polarization angles.

https://dx.doi.org/10.1021/acsami.0c00095
ACS Appl. Mater. Interfaces 2020, 12, 11388−11396

polarization. By measuring the Δf and phase for every polarization scheme, the proposed MB platforms with anisotropic resonances are able to acquire more comprehensive insights into changes in cancer cells. Figure 5 shows the dependence of measured Δf and phase information on cell concentration in terms of two kinds of cancer cells in certain polarization cases. It suggests from Figure 5a,b that although the maximum of Δf are always reached at the highest cell concentration of 5×10^5 cells/mL in all measurements with different polarization schemes, the dependences of Δf on the cell concentration are slightly the same. For example, in the case of a polarization angle of 150°, the Δf roughly experiences a decline and rise stage before and after the concentration of HepG2 cells arrives at 3×10^5 cells/mL. Whereas for A549 cells, the Δf experiences a rise stage before the cell concentration arrives at 1×10^5 cells/mL. Once this concentration is exceeded, the Δf does not increase until the cell concentration is over 3×10^5 cells/mL. In addition, the maximum of Δf maybe diverse for different polarization measurements. When the polarization angle is 60°, the maximum of Δf are up to 145 GHz and 213 GHz for HepG2 and A549 cells, respectively. The variations in Δf indicate that the proposed MBs are able to detect the concentration of cancer cells. The theoretical sensitivity of the designed MBs can reach up to 525 GHz/RIU (see more details in the Supporting Information, Figure S2). While for experimental results, due to the unknown refractive index of cancer cells, it is difficult to obtain the experimental sensitivity. For this reason, we use the A549 cells to evaluate the biosensing ability as a reference of practical sensitivity. Since the Δf was found to be 213 GHz at the cell concentration of 5×10^5 cells/mL, the practical sensitivity was calculated to be $S = \Delta f/\Delta n = 213\ \text{GHz}/(5 \times 10^5)\ \text{cells/mL} = 430\ \text{kHz/cell mL}^{-1}$, which means that an A549 cell per milliliter would lead to the shift of 430 kHz in the resonant frequency. Also, some of the typical features displayed in the correspondence of Δf to the cell concentration may also imply the cell state distinction between different cancer cells in the THz measurements. The complete data could be found in the Supporting Information, Figure S3. The phase information of two kinds of cancer cells supplies additional perspective. Similar to the Δf change, FPS also varied with different polarizations. Obviously, for the polarization angle of 120°, the FPS roughly decreases with the increase in HepG2 concentration, while the A549 cells undergo a steep change at the concentration of 5×10^4 cells/mL. Meanwhile, the FPS exhibits the opposite signs for two kinds of cancer cells. The FPS values of HepG2 cells for all concentrations are bigger than zero, which means the positive sign of FPS. For A549 cells, except for the positive slope at 5×10^4 cells/mL, the negative slopes are exhibited at other concentrations. Such distinct FPS characteristics in two cancer cells are also found in other polarization cases (see the Supporting Information, Figure S3).

From above various dependences of Δf and FPS on cell concentration, it can be found that there is a certain correlation between the polarization and the optical parameters (Δf or FPS) for two kinds of cancer cells. Notably, because the polarization direction is rotated around the MBs, the Δf and the FPS would constitute certain enclosed shapes if the corresponding values located in each polarization direction are connected. Therefore, in order to construct the overall images about the dependence of Δf and FPS on the polarization direction, the hexagonal radar maps are plotted in Figure 6. The Δf radar maps under different cell concentrations are shown in Figure 6a. For convenient comparison, the shapes corresponding to HepG2 and A549 cells are given together and represented by different colors. It is clearly shown from results that no matter which kind of cell is, the area of enclosed shapes covers the biggest at the 5×10^5 cells/mL. Furthermore, the Δf distribution turned out to be anisotropic, which can be inferred from the enclosed shape. For instance, the A549 cells mainly generate a high Δf at the 0° polarization angle when the cell concentration is 3×10^4 cells/mL. Meanwhile, the high Δf appears at the polarization angle of 90° when the cell concentration increases to 5×10^4 cells/mL. The multicriteria feature resulting from polarization-dependent resonances of MB platforms transforms the one-dimensional dependence of Δf on cell concentration into two-dimensional shapes, enhancing its validity to detect small quantities of biological analytes. The most striking results that emerge from the data are shown in Figure 6b. The FPS radar maps between the A549 and HepG2 groups show that the enclosed area of HepG2 cells are always bigger than that of A549 cells in the radar maps, which means that two kinds of cancer cells can be well recognized based on the significant difference in enclosed shapes in these radar maps without any cellular staining process. As seen from the maps of each cell concentration, most of the zone is occupied by the black shape representing the HepG2 cell group. Instead, the red shape representing the A549 cell group only occupies small space. Also, for most cell concentrations, the enclosed shape of A549 cells concentrates on the center of radar maps. The minimum concentration of identification reduces to as low as 1×10^4 cells/mL. Meanwhile, the radar maps displayed from 1×10^4 to 5×10^5 cells/mL mean that such identification can be kept valid in a wide range of cell concentration, covering from 10^4 to 10^5. This remarkable feature insensitive to cell concentration gives strong power to the MB platforms, making it be a new nonimmune biosensing technology to rapidly determine and distinguish the label-free cancer cells in a wide cell concentration range without any antibody introduction. Additionally, this fundamental work shows great potentials in the detection of cancer cells from a new perspective. Based on this technique, we can continue to measure the anisotropic characteristics of other biological cells. For example, by building the data base, the shapes of the cell mixture in radar maps can be decomposed, and thus, the separate features may represent different biological cells.

The majority of studies on the state-of-the-art MB platforms operating in the THz range, as far as we know, mainly focus on their resonant changes in the frequency domain. However, the method of fast Fourier transform (FFT) used in these studies is to extract the frequency component at the cost of losing time domain information, which is critical for metasurface biosensing. In order to overcome this disadvantage and further obtain a more comprehensive information for cancer cell recognition, a new signal processing method was performed in our experiments. Wavelet is a widely used mathematical branch in the signal processing field. The double domains of continuous wavelet transforms (CWT), that is, the time and the frequency domains determine its ability of giving a multiresolving analysis. In CWT, the analyzing function wavelet $\Psi(t)$ serves as basic wave functions to be compared to test signals $f(t)$ by shifting the wavelet at distance b in the time axis and compressing or stretching its waveform in a scale a. The CWT basic definition can be written as

https://dx.doi.org/10.1021/acsami.0c00095
ACS Appl. Mater. Interfaces 2020, 12, 11388−11396

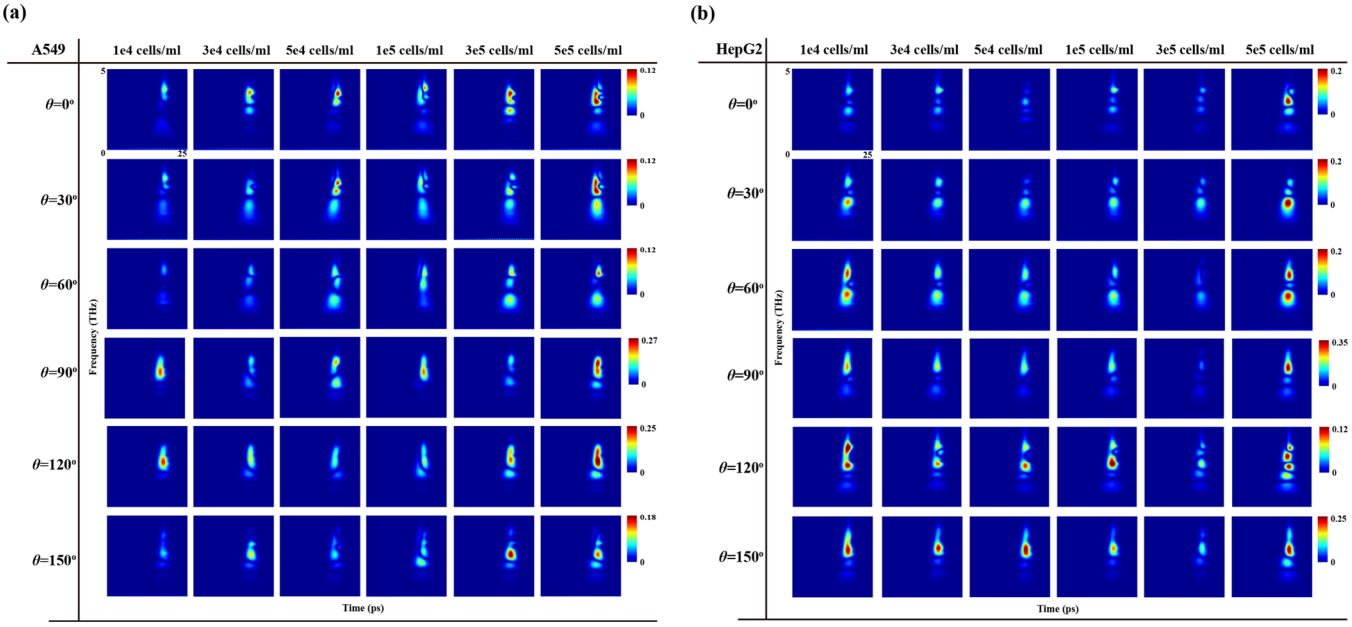

Figure 7. Set of two-dimensional extinction intensity cards of (a) A549 and (b) HepG2 cancer cells at each cell concentration and polarization angle.

$$W_\psi f(a, b) = \int_{-\infty}^{\infty} f(t) \frac{1}{\sqrt{a}} \psi^* \left(\frac{t-b}{a} \right) dt \tag{4}$$

where Ψ^* represents the complex conjugate. Then, given an expression as

$$\psi_{a,b}(t) = \psi_a(t-b) = \frac{1}{\sqrt{a}} \psi \left(\frac{t-b}{a} \right) \tag{5}$$

Based on eq 5, eq 4 can be rewritten as

$$W_\psi f(a, b) = \langle f(t), \psi_{a,b}(t) \rangle \tag{6}$$

Equation 6 suggests that the CWT can be considered as the inner product of the time signals with the wavelet function. More directly, the time signal $f(t)$ is projected on the function of $\Psi_{a,b}(t)$. It means that the one-dimensional signal is transformed into two-dimensional function with two variable parameters: the scale parameter a and the position parameter b. By continuously varying the values of a and b, a series of CWT coefficients are obtained. Since the CWT analysis is a measure of similarity between the basic functions (wavelets) and the test signal, the CWT coefficients C (a, b) are referred to the closeness of the signal to the wavelets at the certain a and b. Here, we select the complex Morlet wavelet as the basic wavelet function, which is expressed as[31]

$$\psi(t) = \frac{1}{\sqrt{\pi f_b}} \times e^{j2\pi fct - \left(t^2/f_b\right)} \tag{7}$$

where f_c and f_b are the central frequency and the bandwidth of the Morlet wavelet, respectively. Here, the f_c and f_b are both selected to be 3 THz. If the measured time signals are taken as $f(t)$, using eqs 6 and 7, joint time-frequency analysis would be achieved in which the parameter a is analogous to frequency and b to the temporal position. In our study, the extinction intensities (un-normalized) of sample mapping on time and frequency domains are acquired by subtracting the intensity of MBs with cells from that of bare samples after the processing of CWT. By dealing with the signals of different concentrations of two kinds of cancer cells under different polarization angles, we can build a set of two-dimensional extinction intensity cards of corresponding cancer cells, as seen in Figure 7. The graphical cards with the detailed information of THz wave−cell interaction can be considered as the standard graphical cards to discriminate the A549 and HepG2 cancer cells through matching the measured extinction intensity graphs of cells and the standard cards. It is observed from the Figure 7a,b that the extinction intensity cards for A549 and HepG2 cancer cells are quite different from each other. For the cell concentration of 1×10^4 cells/mL under a polarization angle of 120°, the strong extinction intensity mainly occurs in one zone distributing from 15.93 to 18.56 ps in the time domain and from 2.43 to 3.71 THz in the frequency domain. While for the HepG2 cells under the same condition, the strong extinction intensity split into two zones in the frequency domain from 2.43 to 2.94 THz and from 3.26 to 4.22 THz. The time domain mainly ranges from 15.65 to 19.02 ps. Additionally, the maximum extinction intensity of HepG2 (~0.12) also differs from that of A549 (~0.25). More distinctions can be found in other intensity cards as well. For instance, the intensity distributions in the frequency domain even split into multiple zones for HepG2 cells under the concentration of 5×10^5 cells/mL while intensity distributions split only into a few zones in the intensity cards for A549 cells. The successful construction of standard extinction intensity indicates that we can identify and determine the label-free cancer cells by matching the measured extinction intensity graphs of cells under all polarization angles and concentrations with corresponding standard cards.

CONCLUSIONS

In summary, we have demonstrated a nonimmune biosensing technology based on anisotropic resonant metasurfaces for antibody-free recognition of cancer cells. The mirror-asymmetric designs of plasmonic SRRs generate extended resonant response to THz waves with the change of

https://dx.doi.org/10.1021/acsami.0c00095
ACS Appl. Mater. Interfaces 2020, 12, 11388−11396

polarization. By measuring corresponding Δf and phase information under different cell concentrations at each polarization case, their dependences on the A549 and HepG2 cancer cell concentration enable the MBs to detect the cell concentrations. Some anomalous features such as the decreasing stage in the Δf with the increase in cell concentration are observed, indicating the possible cell state distinction between different concentrations. Besides, the polarization-dependent hexagonal radar maps of Δf and FPS supply strong multidimensional evidence of cancer cell determination and recognition. When the cell concentration reaches the highest (5×10^5 cells/mL), the Δf in all polarization cases reaches the maximum in our measurements, which are up to 213 GHz for A549 cells and 198 GHz for HepG2 cells. More importantly, the enclosed area of HepG2 cells is always larger than that of A549 cells in the FPS radar maps. Such an insensitive feature to cell concentration contributes to differentiate two kinds of cancer cells by the significant area difference of enclosed shapes in the radar maps without any antibody introduction and cellular staining. This property makes the MB platforms a new potential tool to rapidly distinguish the label-free cancer cells. Finally, a set of standard two-dimensional extinction intensity cards of corresponding cancer cells have been built based on the CWT method. It indicates that we can identify and determine the label-free cancer cells by matching the measured extinction intensity graphs of cells under all polarization angles and concentrations with corresponding standard cards. Although the ability to detect circulating tumor cells is not yet achieved using anisotropic MB platforms, this method also provides some ideas for the detection of circulating cancer cells and points the way for our future research. For example, we can take the signal of biological context as a reference to normalize the measurement signal of samples and calculate the frequency shift, extracting the certain information of cancer cells. Also, the presented method can be combined with other biological means such as biological concentration to minimize the influence of other biological matters, realizing the fast detection of label-free cancer cells in a large number of biological contexts.

EXPERIMENTAL SECTION

Sample Fabrication. In experiments, the PI layer was first spin-coated on the silicon substrate. Subsequently, the patterns of SRRs were fabricated by standard photolithography (ABM Mask Aligner) followed by the deposition of 20 nm Ti and 200 nm Au layers (Denton Vacuum). Finally, the samples were immersed into the HF solution for a few seconds, and the PI layer with patterned SRRs supported upon would be peeled off from the silicon substrate. All measurements are implemented in a THz-TDS system (ADVANTEST TAS7500SU).

Numerical Simulation. In simulation, the full-wave numerical calculations installed in the commercial finite integration package CST Microwave Studio are performed to build the theoretical models. The periodic boundary conditions and the plane wave excitation are adopted. The permittivity ε and tan δ of the PI layer are set to be 3.1 and 0.05, respectively.

Cell Culturing. The whole cultural procedure follows the culturing method of adherent cells.[20,24] The cancer cells were grown at 37°, with 10% concentration of CO_2 (Thermo Fisher Scientific) in the culturing solution, which is mainly consist of Dulbecco's Modified Eagle's medium (Gibco) supplemented with 10% fetal bovine serum (Gibco) and 1% combination of penicillin and streptomycin (Gibco). After the cell morphology reaches a normal state, we added the trypsin−EDTA (Gibco) to digest cells from the walls of culturing bottles followed by the preparation of cell suspension. After the uniform suspension is obtained, the cells are seeded on the MBs and cultured again at the environment mentioned before.

ASSOCIATED CONTENT

Supporting Information

The Supporting Information is available free of charge at https://pubs.acs.org/doi/10.1021/acsami.0c00095.

Measurements and photographs of six concentrations under E_y-polarized THz waves; theoretical sensitivity calculation and linear fitting results; and all dependences of frequency shift Δf and fitted phase slope FPS on cell concentration in terms of two kinds of cancer cells in each polarization case (PDF)

AUTHOR INFORMATION

Corresponding Authors

Lanju Liang − *The Key Laboratory of Opto-Electronics Information and Technology, Institute of Laser and Opto-Electronics, College of Precision Instruments and Opto-Electronics Engineering, Tianjin University, Tianjin 300072, China; School of Opto-Electronic Engineering, Zaozhuang University, Zaozhuang 277160, China;* orcid.org/0000-0002-6936-6815; Email: lianglanju123@163.com

Jianquan Yao − *The Key Laboratory of Opto-Electronics Information and Technology, Institute of Laser and Opto-Electronics, College of Precision Instruments and Opto-Electronics Engineering, Tianjin University, Tianjin 300072, China*; Email: jqyao@tju.edu.cn

Authors

Zhang Zhang − *The Key Laboratory of Opto-Electronics Information and Technology, Institute of Laser and Opto-Electronics, College of Precision Instruments and Opto-Electronics Engineering, Tianjin University, Tianjin 300072, China*

Maosheng Yang − *School of Opto-Electronic Engineering, Zaozhuang University, Zaozhuang 277160, China*

Xin Yan − *School of Opto-Electronic Engineering, Zaozhuang University, Zaozhuang 277160, China*

Xinyue Guo − *School of Electric Power, North China University of Water Resources and Electric Power, Zhengzhou 450045, China*

Jie Li − *The Key Laboratory of Opto-Electronics Information and Technology, Institute of Laser and Opto-Electronics, College of Precision Instruments and Opto-Electronics Engineering, Tianjin University, Tianjin 300072, China;* orcid.org/0000-0002-3400-8241

Yue Yang − *The Key Laboratory of Opto-Electronics Information and Technology, Institute of Laser and Opto-Electronics, College of Precision Instruments and Opto-Electronics Engineering, Tianjin University, Tianjin 300072, China*

Dequan Wei − *School of Opto-Electronic Engineering, Zaozhuang University, Zaozhuang 277160, China*

Longhai Liu − *Advantest (China) Co., Ltd, Shanghai 201203, China*

Jianhua Xie − *Advantest (China) Co., Ltd, Shanghai 201203, China*

Yufei Liu − *College of Optoelectronic Engineering, Chongqing University, Chongqing 400044, China*

Complete contact information is available at:

https://dx.doi.org/10.1021/acsami.0c00095
ACS Appl. Mater. Interfaces 2020, 12, 11388−11396

https://pubs.acs.org/10.1021/acsami.0c00095

Author Contributions

[#]Z.Z. and M.Y. contributed equally to this work.

Notes

The authors declare no competing financial interest.

■ ACKNOWLEDGMENTS

This work was supported by the National key Research and Development Program of China (grant nos. 2017YFB1401203 and 2017YFA0700202), the National Natural Science Foundation of China (grant nos. 61735010 and 61701434), the Natural Science Foundation of Shandong Province (grant nos. ZR2017MF005 and ZR2018LF001), the Programe of Independent and Achievement Transformation plan for Zaozhuang (grant no. 2016GH19), the Funding by Qingchuang Science and Technology Plan of Shandong Universities (2019KJN001), the Open Fund of Key laboratory of Optoelectronic Information Technology, Ministry of Education (Tianjin University), and the Project Special Funding of Taishan Scholar.

■ REFERENCES

(1) Smith, D. R.; Padilla, W. J.; Vier, D. C.; Nemat-Nasser, S. C.; Schultz, S. Composite Medium with Simultaneously Negative Permeability and Permittivity. *Phys. Rev. Lett.* **2000**, *84*, 4184−4187.
(2) Shelby, R. A.; Smith, D. R.; Schultz, S. Experimental Verification of a Negative Index of Refraction. *Science* **2001**, *292*, 77−79.
(3) Smith, D. R.; Pendry, J. B.; Wiltshire, M. C. K. Metamaterials and Negative Refractive Index. *Science* **2004**, *305*, 788−792.
(4) Zhang, X.; Tian, Z.; Yue, W.; Gu, J.; Zhang, S.; Han, J.; Zhang, W. Broadband Terahertz Wave Deflection Based on C-shape Complex Metamaterials with Phase Discontinuities. *Adv. Mater.* **2013**, *25*, 4567−4572.
(5) Shalaev, V. M. Optical Negative-Index Metamaterials. *Nat. Photonics* **2007**, *1*, 41−48.
(6) Yu, N.; Genevet, P.; Kats, M. A.; Aieta, F.; Tetienne, J.-P.; Capasso, F.; Gaburro, Z. Light Propagation with Phase Discontinuities: Generalized Laws of Reflection and Refraction. *Science* **2011**, *334*, 333−337.
(7) Chen, H.; Chan, C. T.; Sheng, P. Transformation Optics and Metamaterials. *Nat. Mater.* **2010**, *9*, 387−396.
(8) Binion, J. D.; Lier, E.; Hand, T. H.; Jiang, Z. H.; Werner, D. H. A Metamaterial-Enabled Design Enhancing Decades-Old Short Backfire Antenna Technology for Space Applications. *Nat. Commun.* **2019**, *10*, 108.
(9) Cui, T. J.; Qi, M. Q.; Wan, X.; Zhao, J.; Cheng, Q. Coding Metamaterials, Digital Metamaterials and Programmable Metamaterials. *Light-Sci. Appl.* **2014**, *3*, No. e218.
(10) Kildishev, A. V.; Boltasseva, A.; Shalaev, V. M. Planar Photonics with Metasurfaces. *Science* **2013**, *339*, 1232009.
(11) Yu, N.; Capasso, F. Flat Optics with Designer Metasurfaces. *Nat. Mater.* **2014**, *13*, 139−150.
(12) Lan, C.; Ma, H.; Wang, M.; Gao, Z.; Liu, K.; Bi, K.; Zhou, J.; Xin, X. Highly Efficient Active All-Dielectric Metasurfaces Based on Hybrid Structures Integrated with Phase-Change Materials: From Terahertz to Optical Ranges. *ACS Appl. Mater. Interfaces* **2019**, *11*, 14229−14238.
(13) Chen, H.-T.; Taylor, A. J.; Yu, N. A Review of Metasurfaces: Physics and Applications. *Rep. Prog. Phys.* **2016**, *79*, No. 076401.
(14) He, Q.; Sun, S.; Xiao, S.; Zhou, L. High-Efficiency Metasurfaces: Principles, Realizations, and Applications. *Adv. Opt. Mater.* **2018**, *6*, 1800415.
(15) Padilla, W. J.; Taylor, A. J.; Highstrete, C.; Lee, M.; Averitt, R. D. Dynamical Electric and Magnetic Metamaterial Response at Terahertz Frequencies. *Phys. Rev. Lett.* **2006**, *96*, 107401.
(16) Sreekanth, K. V.; Dong, W.; Ouyang, Q.; Sreejith, S.; ElKabbash, M.; Lim, C. T.; Strangi, G.; Yong, K.-T.; Simpson, R. E.; Singh, R. Large-Area Silver-Stibnite Nanoporous Plasmonic Films for Label-Free Biosensing. *ACS Appl. Mater. Interfaces* **2018**, *10*, 34991−34999.
(17) Sreekanth, K. V.; Alapan, Y.; ElKabbash, M.; Ilker, E.; Hinczewski, M.; Gurkan, U. A.; de Luca, A.; Strangi, G. Extreme Sensitivity Biosensing Platform Based on Hyperbolic Metamaterials. *Nat. Mater.* **2016**, *15*, 621−627.
(18) Leitis, A.; Tittl, A.; Liu, M.; Lee, B. H.; Gu, M. B.; Kivshar, Y. S.; Altug, H. Angle-Multiplexed All-Dielectric Metasurfaces for Broadband Molecular Fingerprint Retrieval. *Sci. Adv.* **2019**, *5*, No. eaaw2871.
(19) Ahmadivand, A.; Gerislioglu, B.; Manickam, P.; Kaushik, A.; Bhansali, S.; Nair, M.; Pala, N. Rapid Detection of Infectious Envelope Proteins by Magnetoplasmonic Toroidal Metasensors. *ACS Sens.* **2017**, *2*, 1359−1368.
(20) Yan, X.; Yang, M.; Zhang, Z.; Liang, L.; Wei, D.; Wang, M.; Zhang, M.; Wang, T.; Liu, L.; Xie, J.; Yao, J. The Terahertz Electromagnetically Induced Transparency-Like Metamaterials for Sensitive Biosensors in the Detection of Cancer Cells. *Biosens. Bioelectron* **2019**, *126*, 485−492.
(21) Kelp, G.; Arju, N.; Lee, A.; Esquivel, E.; Delgado, R.; Yu, Y.; Dutta-Gupta, S.; Sokolov, K.; Shvets, G. Application of Metasurface-Enhanced Infra-Red Spectroscopy to Distinguish between Normal and Cancerous Cell Types. *Analyst* **2019**, *144*, 1115−1127.
(22) Dayal, G.; Chin, X. Y.; Soci, C.; Singh, R. High-QPlasmonic Fano Resonance for Multiband Surface-Enhanced Infrared Absorption of Molecular Vibrational Sensing. *Adv. Opt. Mater.* **2017**, *5*, 1600559.
(23) Sreekanth, K. V.; Sreejith, S.; Han, S.; Mishra, A.; Chen, X.; Sun, H.; Lim, C. T.; Singh, R. Biosensing with the Singular Phase of an Ultrathin Metal-Dielectric Nanophotonic Cavity. *Nat. Commun.* **2018**, *9*, 369.
(24) Srivastava, Y. K.; Ako, R. T.; Gupta, M.; Bhaskaran, M.; Sriram, S.; Singh, R. Terahertz Sensing of 7 nm Dielectric Film with Bound States in the Continuum Metasurfaces. *Appl. Phys. Lett.* **2019**, *115*, 151105.
(25) Srivastava, Y. K.; Cong, L.; Singh, R. Dual-Surface Flexible THz Fano Metasensor. *Appl. Phys. Lett.* **2017**, *111*, 201101.
(26) Li, Q.; Cong, L.; Singh, R.; Xu, N.; Cao, W.; Zhang, X.; Tian, Z.; Du, L.; Han, J.; Zhang, W. Monolayer Graphene Sensing Enabled by the Strong Fano-Resonant Metasurface. *Nanoscale* **2016**, *8*, 17278−17284.
(27) Nagatsuma, T.; Ducournau, G.; Renaud, C. C. Advances in Terahertz Communications Accelerated by Photonics. *Nat. Photonics* **2016**, *10*, 371−379.
(28) Hendry, E.; Carpy, T.; Johnston, J.; Popland, M.; Mikhaylovskiy, R. V.; Lapthorn, A. J.; Kelly, S. M.; Barron, L. D.; Gadegaard, N.; Kadodwala, M. Ultrasensitive Detection and Characterization of Biomolecules Using Superchiral Fields. *Nat. Nanotechnol.* **2010**, *5*, 783−787.
(29) Zhang, C.; Liang, L.; Ding, L.; Jin, B.; Hou, Y.; Li, C.; Jiang, L.; Liu, W.; Hu, W.; Lu, Y.; Kang, L.; Xu, W.; Chen, J.; Wu, P. Label-free measurements on cell apoptosis using a terahertz metamaterial-based biosensor. *Appl. Phys. Lett.* **2016**, *108*, 241105.
(30) Zhang, Z.; Ding, H.; Yan, X.; Liang, L.; Wei, D.; Wang, M.; Yang, Q.; Yao, J. Sensitive detection of cancer cell apoptosis based on the non-bianisotropic metamaterials biosensors in terahertz frequency. *Opt. Mater. Express* **2018**, *8*, 659−667.
(31) Teolis, A. *Computational Signal Processing with Wavelets*; Birkhauser: Boston, MA, USA 1998.